

---

# MULTI-MODAL CAUSAL INFERENCE WITH DEEP STRUCTURAL EQUATION MODELS

---

**Shachi Deshpande, Zheng Li, Volodymyr Kuleshov**

shachi@cs.cornell.edu, z1634@cornell.edu

kuleshov@cornell.edu

Department of Computer Science, Cornell Tech

New York, NY, 10044

## ABSTRACT

Accounting for the effects of confounders is one of the central challenges in causal inference. Unstructured multi-modal data (images, time series, text) contains valuable information about diverse types of confounders, yet it is typically left unused by most existing methods. This paper seeks to develop techniques that leverage this unstructured data within causal inference to correct for additional confounders that may otherwise not be accounted for. We formalize this task and we propose algorithms based on deep structural equations that treat multi-modal unstructured data as proxy variables. We empirically demonstrate on tasks in genomics and healthcare that unstructured data can be used to correct for diverse sources of confounding, potentially enabling the use of large amounts of data that were previously not used in causal inference.

## 1 Introduction

A central goal of causal inference is to understand from observational data the causal effect of performing an intervention—e.g., the effect of a behavioral choice on an individual’s health (Pearl, 2009). As a motivating example for this work, consider the problem of determining the effect of smoking on an individual’s risk of heart disease.

This problem is complicated by the presence of unobserved confounders: for example, individuals who smoke are more likely be sedentary, which also strongly impacts heart disease risk. If the subject’s lifestyle is available to us as a well-defined feature, we may disentangle its effects from those of smoking (Pearl, 2009). However, most confounders are not easily observed and presented to us as features, making accurate causal inference particularly challenging.

Modern datasets in domains such as medicine or genomics often come with large amounts of *unstructured data*—e.g., medical images, clinical notes, wearable sensor data Bycroft et al. (2018). This data contains strong signal about confounding factors—e.g., wearables data can help identify sedentary individuals. However, most existing methods are not able to naturally leverage this “dark data” for causal inference (Kallus, 2020).

The goal of this paper is to develop novel methods in causal inference that enable correcting for important unobserved confounders from unstructured multi-modal data, such as images and text. For example, given time series from patients’ wearables, our methods may identify important clusters in the data (which may correspond to active and sedentary lifestyles), and use them to disentangle the effects of being sedentary from smoking without ever requiring an explicit featurization of lifestyle.

Specifically, we define multi-modal causal inference, a task that seeks to estimate causal treatment effect given unstructured proxy variables from multiple modalities (images, text). We introduce an approach tailored to this task based on deep structural equations assisted by novel approximate variational inference and learning algorithms (Blei et al., 2017). Our approach enables efficient causal inference with a large set of diverse modalities (some of which may be missing), and also improves over existing deep causal inference methods in a non-multi-modal setting.

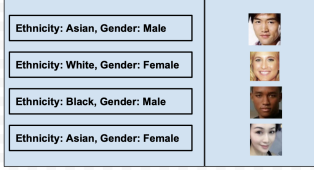


Figure 1: Multimodal Inference. We can use unstructured data like images to infer features like gender, ethnicity, etc using our multimodal architecture.

We examine our methods in a genome-wide association study (GWAS) setting, as well as on new benchmarks that we derive from popular causal inference datasets. We empirically demonstrate that unstructured auxiliary sources of data can be used to correct for latent confounders, which suggests the possibility of using large amounts of data that were previously not used for causal inference.

**Contributions** In summary, this paper makes three contributions: (1) we define multi-modal causal inference, a task in which we rely on unstructured data to correct for unobserved confounders; (2) we propose an approach based on deep structural equations tailored to this problem and we derive specialized variational learning and inference algorithms; (3) we demonstrate empirically that unstructured data can be used to correct for unobserved confounders, potentially enabling the use of large amounts of “dark data” that was previously not used in causal inference.

## 2 Background

A major goal of causal inference is to understand the causal effect of an intervention on a system—e.g., the effect of a treatment on a patient—and correct for the effects of confounding—e.g., the treatment is only given to sick patients and correlates with bad health outcomes.

**Notation** Formally, we are given an observational dataset  $\mathcal{D} = \{(x^{(i)}, y^{(i)}, t^{(i)})\}_{i=1}^n$  consisting of  $n$  individuals, each characterized by features  $x^{(i)} \in \mathcal{X} \subseteq \mathbb{R}^d$ , a binary treatment  $t^{(i)} \in \{0, 1\}$ , and a scalar outcome  $y^{(i)} \in \mathbb{R}$ . We assume binary treatments and scalar outcomes, although our method naturally extends beyond this setting.

We also use  $z^{(i)} \in \mathbb{R}^p$  to model latent confounding factors that influence both the treatment and the outcome. We assume that  $(x^{(i)}, y^{(i)}, t^{(i)}, z^{(i)})$  represent i.i.d. realizations of random variables  $X, Y, T, Z \sim \mathbb{P}$  from a data distribution  $\mathbb{P}$  that decomposes as  $\mathbb{P}(X|Z)\mathbb{P}(Y|Z, T)\mathbb{P}(T|Z)\mathbb{P}(Z)$  (thus  $Z$  is indeed a confounder). We are interested in recovering the true effect of  $T = t$  in terms of its individual and average treatment effects:

$$\bar{Y}[x, t] = \mathbb{E}[Y|X = x, \text{do}(T = t)] \quad (1)$$

$$\text{ITE}(x) = \bar{Y}[x, 1] - \bar{Y}[x, 0] \quad \text{ATE} = \mathbb{E}[\text{ITE}(X)], \quad (2)$$

where  $\text{do}(\cdot)$  denotes an intervention (Pearl et al., 2000).

**Structural Equations** One of the main approaches to causal inference are structural equation models of the form

$$X = f_1(Z, \varepsilon_1) \quad T = f_2(Z, \varepsilon_2) \quad Y = f_3(Z, T, \varepsilon_3), \quad (3)$$

where  $Z \sim p(Z)$  is drawn from a prior and the  $\varepsilon_i$  are noise variables drawn independently from their distributions (Duncan, 2014). Structural equations define a *generative model* of the data. When this model encodes the true dependency structure of  $\mathbb{P}$ , we can estimate the true effect of an intervention by clamping  $T = t$  and drawing samples.

**Deep Structural Equations** Equations 3 can be parameterized with deep neural networks, which yields deep structural equation models. Expressive neural networks may better fit the data and recover the true distribution, which improves causal inference; they also often scale well to large datasets. Such models have been previously used for GWAS analysis (Tran & Blei, 2017) as well as for correcting for proxy variables (Louizos et al., 2017).

## 3 Multi-Modal Causal Inference

Modern datasets in healthcare or genomics often feature large amounts of unstructured data (medical images, clinical notes) that contains strong signal about confounding factors, yet existing causal inference methods do not use this data.

The goal of this paper is to develop methods for leveraging unstructured data within causal inference. We start by formalizing this task as multi-modal causal inference, which seeks to estimate causal treatment effect given unstructured proxy variables from multiple modalities (images, text).

### 3.1 Task Definition

Formally, consider a causal inference dataset  $\mathcal{D} = \{(x^{(i)}, y^{(i)}, t^{(i)})\}_{i=1}^n$  in which  $x^{(i)} = (x_1^{(i)}, x_2^{(i)}, \dots, x_m^{(i)})$  is a vector of  $m$  distinct inputs  $x_j^{(i)} \in \mathcal{X}_j$  (e.g., images, text, time series, etc.). In other words,  $\mathcal{X} = \mathcal{X}_1 \times \dots \times \mathcal{X}_m$ , where each  $\mathcal{X}_j$  corresponds to a space of images, time series, or other unstructured modalities. Some modalities may also be missing at training or inference time.

We assume that the  $x_j^{(i)}$  are i.i.d. realizations of a random variable  $X_j$  with  $X = (X_1, \dots, X_m)$ . We are interested in recovering the true effect of  $T = t$  in terms of the individual and average treatment effects. We are specifically interested in estimating the individual treatment effect (ITE) from arbitrary subsets of modalities  $\mathcal{M} \subseteq \{1, 2, \dots, m\}$ , representing the fact that individuals may be missing data at test time.

$$\bar{Y}[x, t, \mathcal{M}] = \mathbb{E}[Y | \text{do}(T = t), X_j = x_j \text{ for } j \in \mathcal{M}] \quad (4)$$

$$\text{ITE}(x, \mathcal{M}) = \bar{Y}[x, t = 1, \mathcal{M}] - \bar{Y}[x, t = 0, \mathcal{M}] \quad (5)$$

### 3.2 Motivating Applications

To help make this setup more concrete, we define two motivating applications.

**Healthcare** Consider the task of determining the effect of smoking on heart disease from an observational dataset of patients. In modern medical datasets, we may have access to large amounts of *unstructured* data about a patient, e.g., clinician notes, medical images, wearable sensor data, etc. This data can hold crucial information for correcting the effects of confounding variables: for example, raw wearable sensor data can be clustered to uncover sedentary and active groups within the smoker population; this information reveals the effects of an additional confounder, lifestyle.

**Genomics** Consider the problem of understanding the effects of genetic variants via a genome-wide association study (GWAS). Modern GWAS datasets in plants, animals, and humans (Bycroft et al., 2018) feature large amounts of unstructured inputs: clinical notes, medical records, geographical data from the location of the collected samples. This data can be used to correct for environmental confounding. For example, existing plant datasets (Weigel & Mott, 2009) may also contain historical weather data at the collection site (e.g., time series of precipitation, wind strength, etc.). Clustering this data can reveal distinct climatic regions that affect plant phenotypes and whose confounding effects should be corrected for.

## 4 Multi-Modal Deep Structural Equations

Next, we derive models and associated inference and learning algorithms for the task of multi-modal causal inference.

### 4.1 Causal Inference With Deep Structural Equations

Our approach uses deep structural equations to extract confounders found in the multi-modal features  $x_j^{(i)}$ . Using neural networks for this task offers the following benefits.

**Multi-Modality.** Neural networks are especially effective on unstructured data (images, text) (LeCun et al., 1995) via specialized architectures (e.g., convolutions for images). Furthermore, they can make use of *large pre-trained models* such as CLIP (Radford et al., 2021) to leverage information learned in an unsupervised way.

**Accuracy and Flexibility.** Deep learning models are very expressive; on large datasets, neural networks keep improving as they receive more data, while classical methods plateau. This enables learning a model that closely resembles the true data-generating process and correct for confounders more accurately.

**Hardware & Software Support.** Deep learning greatly benefits from specialized hardware (e.g., graphical and tensor processing units (Wang et al., 2019)) and can be used to scale causal inference to very large datasets.

## 4.2 Model Definitions

Parameterizing structural models with neural networks also presents challenges: they induce complex latent variable models that are amenable to efficient approximate inference algorithms only under certain modeling assumption. We present below a specific instantiation of Equations 3 that will yield such efficient algorithms in the next sections.

To simplify presentation, we define our methods in a setting in which  $X$  is continuous, but they also extend to general  $X$  with minimal modifications.

### 4.2.1 Deep Gaussian Structural Equations

We first define Deep Gaussian Structural Equations (DGSEs), a simple model tailored for settings in which there is only one type of auxiliary data  $x$  (i.e.,  $m = 1$  or, alternatively, when all modalities are always present and we concatenate them):

$$\begin{aligned} Z &\sim \mathcal{N}(0_p, I_p) & X &= \mu_X(Z) + \varepsilon_X \cdot \sigma_X(Z) \\ T &= \mathbb{I}[\varepsilon_T < \pi_T(Z)] & Y &= \mu_Y(Z, T) + \varepsilon_Y \cdot \sigma_Y(Z, T), \end{aligned}$$

where the terms  $\varepsilon_X \sim \mathcal{N}(0_d, I_d)$ ,  $\varepsilon_Y \sim \mathcal{N}(0, I)$ , and  $\varepsilon_T \sim U([0, 1])$  are noise variables. The  $\mu, \sigma, \pi$  variables are functions defined by deep neural networks.

These equations define a joint probability of the form

$$p(X, Y, T, Z) = p(Z)p(X|Z)p(T|Z)p(Y|Z, T),$$

where  $p(X|Z)$  and  $p(Y|Z, T)$  are Gaussians whose mean and covariance are parameterized by neural networks  $\mu_X(\cdot), \sigma_X(\cdot), \mu_Y(\cdot), \sigma_Y(\cdot)$  as in Deep Gaussian Latent Variable models (Lawrence & Hyvärinen, 2005), from which we derive our name. The  $p(T|Z)$  is a conditional Bernoulli parameterized by a neural network  $\pi_T : \mathbb{R}^p \rightarrow [0, 1]$ . These modeling choices will shortly enable us to apply stochastic variational inference algorithms.

**Neural Architectures** In our experiments, the models  $\pi_T, \mu_Y, \sigma_Y$  follow the architecture of Louizos et al. (2017) (see Appendix B). The model for  $X$  is highly domain-specific. When using a multi-layer perceptron, we recover exactly the CE-VAE model of Louizos et al. (2017). However, certain modalities will benefit from specialized architectures, e.g., a convolutional model for images and a recurrent one for time series. See the Appendix B for details.

### 4.2.2 Deep Multi-Modal Structural Equations

Next, we consider the full case where  $X = (X_1, \dots, X_m)$  and we define our full model in this regime. We introduce Deep Multi-Modal Structural Equations (DMSEs), a model of the form:

$$\begin{aligned} Z &\sim \mathcal{N}(0_p, I_p) & X_j &= \mu_{X_j}(Z) + \varepsilon_{X_j} \cdot \sigma_{X_j}(Z) \quad \forall j \\ T &= \mathbb{I}[\varepsilon_T < \pi_T(Z)] & Y &= \mu_Y(Z, T) + \varepsilon_Y \cdot \sigma_Y(Z, T), \end{aligned}$$

where the  $\varepsilon_i \sim \mathcal{N}(0, I)$ . The  $\mu, \sigma, \pi$  variables are functions defined by deep neural networks.

These equations define a joint probability of the form

$$p(X, Y, T, Z) = p(Z)p(T|Z)p(Y|Z, T) \prod_{j=1}^m p(X_j|Z),$$

where the  $p(X_j|Z)$  are Gaussians whose mean and covariance are parameterized by neural networks, and the remaining distributions are the same as in our initial model. Note that we make the natural modeling assumption that each auxiliary modality is independent of the others conditioned on  $Z$ . Figure 2 shows the dependencies. As before, the architecture for each  $p(X_j|Z)$  will be domain-dependent.

## 4.3 Approximate Inference and Learning Algorithms

### 4.3.1 Deep Gaussian Structural Equations

The DGSE model induces a joint probability  $p(X, Y, T, Z)$ , which allows us to fit its parameters using stochastic variational inference by optimizing the ELBO

$$\sum_{i=1}^n \mathbb{E}_q \left[ \log p(x^{(i)}, y^{(i)}, t^{(i)}, z) - \log q(z|x^{(i)}, y^{(i)}, t^{(i)}) \right],$$

where  $q(z|x, y, t)$  is an approximate variational posterior. When  $q$  consists of fully connected layers, we use the architecture of Louizos et al. (2017); when  $x$  consists of unstructured data, convolutional, recurrent, or self-attention architectures are preferable, and lead to different designs for  $q$ , which we discuss in the Appendix B.

We optimize the above objective using gradient descent, applying the reparameterization trick to estimate the gradient. We compute the counterfactual  $\hat{Y}$  for each  $t$  using auxiliary inference networks. See the Appendix B for the full derivation the procedure.

### 4.3.2 Deep Multi-Modal Structural Equations

In the full multi-modal setting, the  $X_j$  are conditionally independent given  $Z$  (Figure 2), which enables us to apply more efficient algorithms inspired by Wu & Goodman (2018). These algorithms offer the following improvements: (1) we may perform learning, inference, and causal estimation with missing modalities  $X_j$ ; (2) the process for performing causal inference is simpler than in DGSE and does not require training auxiliary inference networks.

The DMSE model induces a joint probability  $p(X, Y, T, Z)$ , which enables us to optimize the following multimodal ELBO objective using stochastic variational inference.

$$\text{ELBO}_X = \sum_{i=1}^n \mathbb{E}_q \left[ \sum_{j=1}^m \log p(x_j^{(i)}, z) + \log p(y^{(i)}, t^{(i)}, z) - \log q(z|x^{(i)}, y^{(i)}, t^{(i)}) \right],$$

where  $q(z|x^{(i)}, y^{(i)}, t^{(i)})$  is the approximate variational posterior. We assume a total of  $m$  modalities.

We may use the independence structure of  $p$  (Figure 2) to derive a structured form for  $q$ . First, observe that  $p(z|x, t, y) \propto (p(z|t, y) \prod_{j=1}^m p(z|x_j)) / \prod_{j=1}^{m-1} p(z)$ . This implies that the structure of an ideal  $q$  is  $q(z|x, t, y) \propto (q(z|t, y) \prod_{j=1}^m q(z|x_j)) / \prod_{j=1}^{m-1} p(z)$ . Inspired by this decomposition, we create modality-specific inference networks  $\tilde{q}(z|t, y)$  and  $\tilde{q}(z|x_j)$  such that  $q(z|x_j) = \tilde{q}(z|x_j)p(z)$  and  $q(z|t, y) = \tilde{q}(z|t, y)p(z)$ , which define a joint posterior of the form

$$q(z|x, y, t) \propto p(z) \tilde{q}(z|y, t) \prod_{j=1}^m \tilde{q}(z|x_j). \quad (6)$$

This network can be seen as a product of experts (PoE) (Wu & Goodman, 2018).

Computing the above  $q$  in closed form is not always possible. However, we know that a product of Gaussians with means  $\mu_i$  and covariances  $V_i$  is  $\mu = (\sum \mu_i T_i) / (\sum T_i)$  and  $V = (\sum_i T_i)^{-1}$ , where  $T_i = 1/V_i$ . Since  $p(z)$ ,  $q(z|t, y)$  and  $q(z|x_j)$  are Gaussians, computing  $q(z|x, t, y)$  for any subset of modalities is possible without having to train an inference network for each subset of modalities separately. As in the case of DGSE, every component of  $q$  can be designed differently depending on whether  $x$  represents structured or unstructured data.

**Handling Missing Modalities** Training this architecture with a full set of modalities will not necessarily yield good single-modality inference networks, while training with each modality separately will prevent the network from learning how the modalities are related to each other. Hence, we train our model with a sub-sampled ELBO objective (Wu & Goodman, 2018) that is computed on the full set of modalities, each individual modality, and a few subsets of modalities together. For this, we randomly pick at each gradient step  $s$  non-empty subsets  $\{\mathcal{M}_k\}_{k=1}^s$  of the set of modalities  $\mathcal{M}_k \subseteq \{1, 2, \dots, m\} \forall k$ . The resulting objective is  $\text{ELBO}_X + \sum_{j=1}^m \text{ELBO}_{\{j\}} + \sum_{k=1}^s \text{ELBO}_{\mathcal{M}_k}$ , where

$$\text{ELBO}_{\mathcal{M}} = \sum_{i=1}^n \mathbb{E}_q \left[ \sum_{j \in \mathcal{M}} \log p(x_j^{(i)}, z) + \log p(y^{(i)}, t^{(i)}, z) - \log(p(z) \tilde{q}(z|y^{(i)}, t^{(i)}) \prod_{j \in \mathcal{M}} \tilde{q}(z|x_j^{(i)})) \right]$$

**Computing Treatment Effects** Given a subset of modalities  $\mathcal{M}$ , we can compute the ATE as  $\mathbb{E}(\text{ITE}(x, \mathcal{M}))$ , where  $\text{ITE}(x, \mathcal{M}) = \bar{Y}[x, t = 1, \mathcal{M}] - \bar{Y}[x, t = 0, \mathcal{M}]$  and

$$\begin{aligned} \bar{Y}[x, t = t', \mathcal{M}] &= \int_z p(y, t = t' | z) p(z|x) dz \\ &\approx \int_z (p(y, t = t' | z) p(z) \prod_{j=1}^m \tilde{q}(z|x_j)) dz \end{aligned}$$

Note that this model does not require training additional auxiliary networks.

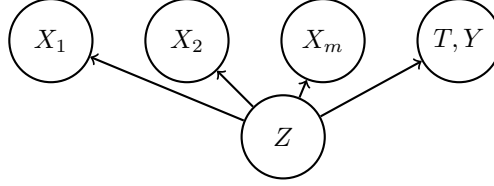


Figure 2: Graphical Model for Multimodal Structural Equations

Table 1: Treatment effect estimation on the synthetic demonstration dataset. The DGSE model demonstrates better generalization and better supports the addition of an unstructured image modality.

	SETTING	$\varepsilon_{ATE}$ (TRAIN)	$\varepsilon_{ATE}$ (TEST)
CAUSAL	BINARY	0.003	0.013
	IMAGE	0.011	0.012
NON-CAUSAL	SETTING	$\varepsilon_{ATE}$ (TRAIN)	$\varepsilon_{ATE}$ (TEST)
	BINARY	0.002	0.018
	IMAGE	0.008	0.022

## 5 Experimental Results

### 5.1 Synthetic Demonstration Dataset

We start with a demonstration that provides intuition for how unstructured proxy variables can be used to uncover and correct the effects of latent confounders. The following small-scale synthetic setup is derived from Louizos et al. (2017) and involves binary variables  $y, t, z, x$ , which correspond, respectively, to the outcome, treatment, confounder, and proxy variables. The data distribution  $\mathbb{P}$  over  $y, t, z, x$  is defined as follows:

1.  $\mathbb{P}(z = 1) = \mathbb{P}(z = 0) = 0.5$
2.  $\mathbb{P}(x = 1|z = 1) = \mathbb{P}(x = 0|z = 0) = \rho_x = 0.5$
3.  $\mathbb{P}(t = 1|z = 1) = \mathbb{P}(t = 0|z = 0) = \rho_t = 0.3$
4.  $y = t \oplus z$

where  $0 < \rho_x, \rho_t < 1$  are parameters. Crucially, we introduce an unstructured proxy variable  $\mathbf{X}$  that represents an “image version” of  $x$ . The variable  $\mathbf{X}$  will be a random MNIST image of a zero or one, depending on whether  $x = 0$  or  $x = 1$ . Formally,  $\mathbf{X}$  is distributed as follows:

- $\mathbb{P}(\mathbf{X}|x = 1)$  is uniform over MNIST images of “1”
- $\mathbb{P}(\mathbf{X}|x = 0)$  is uniform over MNIST images of “0”

We show in Appendix A that this setup requires using a causal model. Specifically, a standard non-causal model of  $\mathbb{P}(y | \mathbf{X}, t)$  perfectly trained using supervised learning recovers the true ATE only when  $\rho_t = \rho_x = 0.5$ .

We fit DGSE models to 10000 training data points of  $\{x, y, t\}$  (the BINARY setting) as well as of  $\{\mathbf{X}, y, t\}$  (the IMAGE setting). We note the Average Treatment Effect (ATE) on 600 test datapoints sampled independently from  $\mathbb{P}$  and we report results in Table 1.

We find that causal models are indeed necessary to solve this task. Furthermore, the DGSE model is able to extract confounding signal from unstructured proxy variables  $\mathbf{X}$  and perform as well as models trained on the featurized proxy variables  $x$ .

### 5.2 Infant Health and Development Project (IHDP)

The Infant Health and Development Project (IHDP) is a popular benchmark for causal inference algorithms (Hill, 2011) that contains the outcomes of comprehensive early interventions for premature, low birth weight infants. The data corresponding to non-white mothers in the treated set of children is removed so that causal effect of the intervention cannot be estimated directly. The column corresponding to mother’s race is removed so that this confounder cannot be obtained directly from the input. We consider 100 replicates of this dataset, where the output is simulated according to setting ‘A’ of NPCI package (Dorie, 2021).

**The IHDP-Full Setting** There are 25 input features in this experimental setting. We train a DGSE model on each replicate with a 63/27/10 ratio of training, validation and test dataset size. We set the latent dimension to be 20 units and the number of hidden layers to be 2. We report the absolute error in ATE produced by DGSE in Table 2.

**The IHDP-Mini Setting** Our goal is to create a benchmark for multi-modal causal inference based on IHDP in which we can replace certain features with their "unstructured version". Our first step towards this is to select a subset of the 25 proxy features available in IHDP in order to magnify their relative important and accurately measure the effects of their removal. We looked at F-statistics and mutual information between selected features and the target variable in the initial 100 replicates of the IHDP dataset. With some experimentation, we have chosen 9 input attributes and we refer to this setting as IHDP-Mini. The chosen attributes are mentioned in Appendix C.

**Adding Unstructured Modalities to IHDP-Mini** One of the 9 attributes in IHDP-Mini corresponds to the baby's gender. To design a multi-modal experiment, we replace the attribute 'baby's gender' with an image of a child between ages 3 to 8 years, drawn from the UTK dataset (Zhang et al., 2017). See Figure 1 for examples of how images from the UTK dataset can replace features. We use CLIP embeddings (Li et al., 2022) of these images to produce a smaller 512-dimensional embedding corresponding to a given image. Our use of pre-trained embeddings demonstrates the ability of our approach to integrate with external sources of information trained using unsupervised or self-supervised learning. We train and evaluate models on this dataset where the image 'replaces' the attribute 'baby's gender' (8 ATTRS + IMAGE). We also consider two other settings for comparison: a) the original 'baby's gender' attribute is included (9 ATTRS) and b) baby's gender is dropped from the reduced set of input features (8 ATTRS).

We also demonstrate that our pre-trained embeddings contain useful signal by building a neural network model that predicts a baby gender from an image's CLIP embedding. We discuss this further in the Appendix D.

Table 2: Treatment effects on IHDP Dataset. Using a reduced set of features in the IHDP Mini setting produces comparable absolute ATE errors as the degradation is small. Numbers in round braces indicate standard deviations. Since this is a simulated dataset, we can directly compute the treatment effect using the simulated factual and counterfactual outputs. ATE error is the absolute difference between true ATE and predicted ATE.

MODELS	INPUT	$\varepsilon_{ATE}$ (TRAIN+VAL)	$\varepsilon_{ATE}$ ERROR(TEST)
DGSE	FULL	0.289 (0.027)	0.358 (0.041)
OLS	FULL	0.535 (0.089)	0.718 (0.132)
DGSE	MINI	0.364 (0.053)	0.440 (0.064)

Table 3: Multimodal Experiments on IHDP Dataset: We see that removing baby's gender (8 attrs) from IHDP-Mini setting (9 attrs) shows increase in average ATE error, demonstrating that this attribute is important in estimating treatment effect. Replacing this attribute with corresponding image embedding (8 attrs + image) shows some increase in ATE error but is much better than dropping this modality altogether (8 attrs). Similar behavior is also shown by OLS2 on test dataset, however the ATE errors produced by our model are better overall. The CFRNet baseline does not capture image modalities well.

SETTING	$\varepsilon_{ATE}$ (TRAIN+VAL)	$\varepsilon_{ATE}$ ERROR(TEST)
<b>DEEP STR EQNS</b>		
9 ATTRS	0.152 (0.014)	0.244 (0.028)
8 ATTRS	0.155 (0.014)	0.264 (0.030)
8 ATTRS + IMAGE	0.148 (0.014)	0.247 (0.031)
<b>CFRNET</b>		
9 ATTRS	0.342 (0.043)	0.474 (0.070)
8 ATTRS	0.321 (0.037)	0.442 (0.066)
8 ATTRS + IMAGE	0.363 (0.046)	0.463 (0.063)
<b>OLS2</b>		
9 ATTRS	0.197 (0.022)	0.319 (0.039)
8 ATTRS	0.204 (0.024)	0.333 (0.043)
8 ATTRS + IMAGE	0.211 (0.021)	0.319 (0.037)

Table 4: Multimodal Experiments on STAR Dataset: Removing student gender and ethnicity (6 attrs) shows increased ATE errors when compared with retaining these attributes (8 attrs), signaling that these two attributes are important for predicting treatment effect. When we replace this with corresponding image of a child, we see that there is no such degradation in ATE estimation. CFRNet shows similar behavior, however the difference in average ATE error across setups is smaller. The true treatment effect can be estimated directly since the original dataset corresponds to a randomized controlled trial. Hence, it is possible to compute ATE error as the absolute difference between true ATE estimate and the ATE as predicted by the model.

SETTING	$\epsilon_{ATE}$ (TRAIN+VAL)	$\epsilon_{ATE}$ ERROR(TEST)
<b>DEEP STR EQNS</b>		
8 ATTRS	36.479 (1.770)	34.039 (2.336)
6 ATTRS	43.682 (1.520)	40.651 (2.425)
6 ATTRS + IMAGE	35.581 (1.723)	33.654 (2.476)
<b>CFRNET</b>		
8 ATTRS	61.835 (1.025)	25.436 (2.332)
6 ATTRS	62.055 (1.001)	25.649 (2.339)
6 ATTRS + IMAGE	61.350 (1.109)	25.219 (2.313)

**Results** As seen in Table 3, we observe that the degradation in ATE error as produced by replacing the baby’s gender by a photograph is lower as compared to removing the attribute entirely. This shows that our deep structural equation models able to leverage signal found in the unstructured image modality. Our results lend further support to the fact that we can incorporate unstructured modalities such as images in causal inference with the help of deep neural network models.

We compare these results with a simple Ordinary Least Squares model (OLS2) baseline as described by Shalit et al. (2017) to predict treatment effect. Here, we train one OLS model on treated population and another OLS model on untreated population. Treatment effect can be estimated by computing the difference between the predictions of these two models following 5. OLS2 shows a similar behavior when replacing baby’s gender with corresponding image, however ATE errors are generally worse as compared to ATE error produced by DGSE. We also compare this with Counterfactual Regression Network (CFRNet) (Johansson et al., 2018b) baseline. However CFRNet did not show increase in average ATE error after dropping baby’s gender.

### 5.3 Student-Teacher Achievement Ratio

The Student-Teacher Achievement Ratio (STAR) experiment (Achilles et al., 2008) studied the effect of class size on the performance of students. We consider small class size as treatment, while regular class size implies absence of treatment. We define the outcome variable as the sum of the reading and math scores of a student. Thus, the treatment effect is the change in total score of the student in response to small class size as intervention. We ‘derandomize’ this dataset by removing 80% of the data corresponding to white students in the treated population. The dataset (Achilles et al., 2008) has 15 input attributes. Similar to the IHDP experiment, we select a subset of these attributes to increase the relative importance of each individual attribute while predicting treatment effects. With some experimentation, we select a total of 8 attributes as input to DGSE. Further details on these attributes can be found in the Appendix C.

**Adding Unstructured Modalities to STAR** We create a second benchmark for multi-modal causal inference derived from STAR in which we replace features with unstructured inputs that contain the same information as their featurized versions. Our experimental setup is similar to that used in the IHDP dataset: we replace the attributes corresponding to the student’s ethnicity and gender by selecting an image of a child with the same ethnicity and gender from the UTK dataset. See Figure 1 for examples of how images from the UTK dataset can replace features. We evaluate the quality of CLIP embeddings with respect to predicting gender and ethnicity by training a simple neural network for this task. We discuss this further in Appendix D.

In Table 4, we show that replacing gender and ethnicity attributes with the corresponding image improves ATE errors as compared to dropping these two attributes entirely. This shows that we can use an image to extract multiple attributes while doing causal inference. The CFRNet baseline shows a similar behavior, but the difference between average ATE errors across different setups is small.

## 5.4 Genome-Wide Association Studies

Genome-Wide Association Studies (GWASs) attempt to determine the association between genetic variation and a specific phenotype. We construct an experiment in the GWAS setting to demonstrate the applicability of our algorithms to another unstructured modality: genomic data.

The causal inference task consists in understanding the effects of SNPs (which act like treatments) on the phenotype. However, this task is complicated by ancestry-based confounding. Consider a plant dataset in which individuals come from two distinct populations: if population A comes from an environment that influences the outcome, every SNP that is characteristic of population A (e.g., red flowers) will appear causal for the outcome. We apply our multi-modal causal inference algorithms to correct for this confounding from unstructured genomic data.

**Data and Task** We use the SNP (Single Nucleotide Polymorphism) data for *Arabidopsis Thaliana* plants from the 1001 Genomes Project (Weigel & Mott, 2009). Each plant is associated with a country in which it was grown. We construct a causal inference task in which we seek to predict the GDP  $y$  of that country from a plant's SNPs  $t$ . Obviously this should not be possible: SNPs should not affect GDP and are not causal. However, because the genomes of plants from the same country are similar, there exist spurious correlation caused by latent subpopulation groups  $z$ . Our goal is to detect and correct of these confounding effects from genomic data  $x$  (vectors of SNP values).

**Baselines** We subsample 20% of the SNPs evenly from a given input genome and use the LIMIX library (Lippert et al., 2014) to perform GWAS. Principal Component Analysis (PCA) is a standard technique to correct for confounding in such a setup (Price et al., 2006). PCA is performed over the input SNP data. The top PCA components are concatenated with the input SNPs and GWAS performed over this corrects for the confounding to some extent. We also compare vs. a linear model with no correction for confounding.

**Setup** We apply our deep structural equations framework for correcting the effects of confounding. We fit a DGSE model in two stages: (1) first, we only fit the model of  $p(X|Z)$  using the DGSE ELBO objective; (2) then we fit  $p(Y|Z, T)$  with a fixed  $Z$  produced by the auxiliary model  $q(Z|X)$ . We found this two-step procedure to produce best results. The subsampled SNPs corresponding to each genome are taken as input  $X$ . The encoder and decoder use a single hidden layer of 256 units while a 10-dimensional latent variable  $Z$  is used. This network is optimized using ClippedAdam with learning rate of 0.01, further reduced exponentially over 20 training epochs. The confounding variable for each genome can now be computed as latent representation produced by the VAE. To measure the success of confounding correction, we compute the  $R^2$  values between the true GDP of the region and the GDP output as predicted via our model and the baselines. If we have corrected for confounding, then we should get low  $R^2$  values.

**Results** The DGSE model learns a complex non-linear mapping between latent factors  $z$  and genomic data  $x$ ; as such it can recover and correct for precise population structure that a linear model like PCA cannot. In Table 5, we see the effect of extracting confounding variables using DGSE as opposed to using the standard PCA technique. We can see that the  $R^2$  values produced using DGSE for extracting confounders are closer to 0 as compared to using PCA. This experiment shows that neural network architectures are effective in dealing with the complex modality corresponding to genomic data while correcting for confounding.

Table 5: Comparison of PCA and DGSE to extract confounders. DGSE leads to better correction of confounding as demonstrated by  $r^2$  values closer to zero. PCA produces better  $r^2$  values as compared to simple linear model that does not correct for confounding, but DGSE can learn complex, non-linear relationships between the input SNPs to extract the confounding variable better. The ELBO score computed by VAE underlying DGSE is better as compared to the likelihood assigned by probabilistic PCA to the test dataset

SETTING	$R^2$	SCORE
DEEP STR EQNS (OURS)	0.079 (0.027)	20616.3 (80.6)
PCA	0.111 (0.010)	79224.3 (13.9)
LINEAR MODEL	0.665 (0.012)	-

## 5.5 Multimodal Experiments With Missing Modalities

We also demonstrate the ability of the DMSE model to handle missing data. Recall that our IHDP and STAR benchmarks involve two modalities: images (e.g., baby's gender in IHDP) and tabular data (e.g., the remaining features). We compare DMSE and DGSE models on these datasets when some of the modalities may be missing.

For DMSE, we define two different modalities  $X_1$  and  $X_2$  for the tabular and image modalities respectively. For DGSE, we concatenate the image embedding to the tabular modality while training the network. We evaluate ATE while randomly dropping 50% of the images. DMSE utilizes its product-of-experts inference network to approximate the posterior distribution when modalities are missing. DGSE cannot do this, and we resort to feeding it a vector of zeros when an image is missing. Table 6 shows that DMSE produces improved ATE estimates as compared to the DGSE model. This demonstrates that DMSE can handle missing modalities better.

We perform a similar experiment on the STAR dataset. Recall that there are two modalities: images corresponding to student’s gender and ethnicity and tabular data corresponding to the remaining 6 features in STAR. We train DGSE and DMSE on this dataset and randomly drop 50% of the student images while computing ATE estimates using these two models. In Table 7, we see that DMSE produces better ATE estimates as compared to DGSE. This further shows that DMSE better supports missing modalities.

Table 6: Multimodal Experiments on IHDP Dataset comparing DMSE and DGSE methods. When the child’s photo is missing, DMSE still produces reasonable ATE errors as it can compute the latent representation on a subset of modalities better as compared to DMSE

SETTING	$\varepsilon_{ATE}$ (TRAIN+VAL)	$\varepsilon_{ATE}$ ERROR(TEST)
DMSE	0.433 (0.057)	0.627 (0.094)
DGSE	0.794 (0.308)	1.080 (0.337)

Table 7: Multimodal Experiments on STAR Dataset comparing DMSE and DGSE methods. When the student’s photo is missing, DMSE can still compute causal effects reasonably as compared to the DGSE method.

SETTING	$\varepsilon_{ATE}$ (TRAIN+VAL)	$\varepsilon_{ATE}$ ERROR(TEST)
DMSE	32.575 (1.634)	33.743 (1.890)
DGSE	59.102 (4.734)	60.152 (4.788)

## 6 Related Work

Pearl (2010) describes structural equation model to mathematically represent the relations between variables for studying causality, extending the idea from linear models to non-parametric models and graphs. In observational studies, measuring all confounders is not possible due to which measuring proxies and using them correctly to recover the causal effect is important Wooldridge (2009); Pearl (2012); Greenland & Lash.; Cai & Kuroki (2012); Montgomery et al.; Wang et al. (2018). Louizos et al. (2017) use variational auto-encoders to estimate confounders in a proxy-rich setting. Representation learning in causal inference has been studied by Johansson et al. (2018b;a; 2019) and Schölkopf et al. (2021). Naoki et al. (2018) and Veitch et al. (2020) estimate causal effects on text modality using neural networks. Veitch et al. (2019) estimate causal effects on network graphs as modality. Wu & Goodman (2018) propose multimodal variational auto-encoders to learn joint representations between multiple modalities.

Genome-Wide Association Studies (GWASs) (Uffelmann et al., 2021; Bush & Moore, 2012) are used to determine the association between genetic variations and a phenotype. Principle Components Analysis (PCA) is one of the main ways to correct for confounding in GWAS (Price et al., 2006; Wang et al., 2013).

## 7 Discussion and Conclusion

We propose an approach based on deep structural equations to utilize useful data present in unstructured form to perform causal inference. This can enable us to incorporate large amounts unstructured data that was previously unused. We perform multi-modal causal inference on benchmark datasets to demonstrate that unstructured data in the form of images can be used to estimate causal effect. We also demonstrate superior extraction of confounding variables from SNP data as a modality. We show that deep structural equations can be used to design architectures for causal inference on such multimodal datasets. Deep multimodal structural equations also allow us to perform causal inference on data with missing modalities.

## References

Achilles, C., Bain, H. P., Bellott, F., Boyd-Zaharias, J., Finn, J., Folger, J., Johnston, J., and Word, E. Tennessee's Student Teacher Achievement Ratio (STAR) project, 2008. URL <https://doi.org/10.7910/DVN/SIWH9F>.

Blei, D. M., Kucukelbir, A., and McAuliffe, J. D. Variational inference: A review for statisticians. *Journal of the American statistical Association*, 112(518):859–877, 2017.

Bush, W. S. and Moore, J. H. Chapter 11: Genome-wide association studies. *PLOS Computational Biology*, 8(12):e1002822, 2012. doi: 10.1371/journal.pcbi.1002822. URL <https://app.dimensions.ai/details/publication/pub.1016451804>.

Bycroft, C., Freeman, C., Petkova, D., Band, G., Elliott, L. T., Sharp, K., Motyer, A., Vukcevic, D., Delaneau, O., O'Connell, J., et al. The uk biobank resource with deep phenotyping and genomic data. *Nature*, 562(7726):203–209, 2018.

Cai, Z. and Kuroki, M. On identifying total effects in the presence of latent variables and selection bias, 2012.

Dorie, V. Non-parametrics for causal inference, 2021. URL <https://github.com/vdorie/npci>.

Duncan, O. D. *Introduction to structural equation models*. Elsevier, 2014.

Greenland, S. and Lash., T. Bias analysis. In *Modern epidemiology*.

Hill, J. L. Bayesian nonparametric modeling for causal inference. *Journal of Computational and Graphical Statistics*, 20(1):217–240, 2011.

Hochreiter, S. and Schmidhuber, J. Long short-term memory. *Neural computation*, 9(8):1735–1780, 1997.

Johansson, F. D., Kallus, N., Shalit, U., and Sontag, D. Learning weighted representations for generalization across designs, 2018a.

Johansson, F. D., Shalit, U., and Sontag, D. Learning representations for counterfactual inference, 2018b.

Johansson, F. D., Sontag, D., and Ranganath, R. Support and invertibility in domain-invariant representations, 2019.

Kallus, N. Deepmatch: Balancing deep covariate representations for causal inference using adversarial training. In *International Conference on Machine Learning*, pp. 5067–5077. PMLR, 2020.

Lawrence, N. and Hyvärinen, A. Probabilistic non-linear principal component analysis with gaussian process latent variable models. *Journal of machine learning research*, 6(11), 2005.

LeCun, Y., Bengio, Y., et al. Convolutional networks for images, speech, and time series. *The handbook of brain theory and neural networks*, 3361(10):1995, 1995.

Li, M., Xu, R., Wang, S., Zhou, L., Lin, X., Zhu, C., Zeng, M., Ji, H., and Chang, S.-F. Clip-event: Connecting text and images with event structures. *arXiv preprint arXiv:2201.05078*, 2022.

Lippert, C., Casale, F. P., Rakitsch, B., and Stegle, O. Limix: genetic analysis of multiple traits. *BioRxiv*, 2014.

Louizos, C., Shalit, U., Mooij, J., Sontag, D., Zemel, R., and Welling, M. Causal effect inference with deep latent-variable models. *arXiv preprint arXiv:1705.08821*, 2017.

Montgomery, M., Gragnolati, M., Burke, K., and et al. Measuring living standards with proxy variables.

Naoki, E., Christian, J. F., Justin, G., Margaret, E. R., and Brandon, M. S. How to make causal inferences using texts, 2018.

Pearl, J. *Causality*. Cambridge university press, 2009.

Pearl, J. An introduction to causal inference., 2010.

Pearl, J. On measurement bias in causal inference, 2012.

Pearl, J. et al. Models, reasoning and inference. *Cambridge, UK: Cambridge University Press*, 19, 2000.

Price, A., Patterson, N., Plenge, R., Weinblatt, M., NA, S., and D., R. Principal components analysis corrects for stratification in genome-wide association studies., 2006.

Radford, A., Kim, J. W., Hallacy, C., Ramesh, A., Goh, G., Agarwal, S., Sastry, G., Askell, A., Mishkin, P., Clark, J., et al. Learning transferable visual models from natural language supervision. *arXiv preprint arXiv:2103.00020*, 2021.

Schölkopf, B., Locatello, F., Bauer, S., Ke, N. R., Kalchbrenner, N., Goyal, A., and Bengio, Y. Towards causal representation learning. *CoRR*, abs/2102.11107, 2021. URL <https://arxiv.org/abs/2102.11107>.

Shalit, U., Johansson, F. D., and Sontag, D. Estimating individual treatment effect: generalization bounds and algorithms, 2017.

Tran, D. and Blei, D. M. Implicit causal models for genome-wide association studies. *arXiv preprint arXiv:1710.10742*, 2017.

Uffelmann, E., Huang, Q., Munung, N., and et al. Genome-wide association studies., 2021.

Veitch, V., Wang, Y., and Blei, D. M. Using embeddings to correct for unobserved confounding in networks, 2019.

Veitch, V., Sridhar, D., and Blei, D. M. Adapting text embeddings for causal inference, 2020.

Wang, K., Hu, X., Peng, Y., and Hum, H. An analytical comparison of the principal component method and the mixed effects model for association studies in the presence of cryptic relatedness and population stratification., 2013.

Wang, M., Zhi, G., and Eric, T. T. Identifying causal effects with proxy variables of an unmeasured confounder, 2018.

Wang, Y. E., Wei, G.-Y., and Brooks, D. Benchmarking tpu, gpu, and cpu platforms for deep learning. *arXiv preprint arXiv:1907.10701*, 2019.

Weigel, D. and Mott, R. The 1001 genomes project for arabidopsis thaliana. *Genome biology*, 10(5):1–5, 2009.

Wooldridge, J. M. On estimating firm-level production functions using proxy variables to control for unobservables. *Economics Letters*, 104(3):112–114, 2009. ISSN 0165-1765. doi: <https://doi.org/10.1016/j.econlet.2009.04.026>. URL <https://www.sciencedirect.com/science/article/pii/S0165176509001487>.

Wu, M. and Goodman, N. Multimodal generative models for scalable weakly-supervised learning. *arXiv preprint arXiv:1802.05335*, 2018.

Zhang, Z., Song, Y., and Qi, H. Age progression/regression by conditional adversarial autoencoder. In *Proceedings of the IEEE conference on computer vision and pattern recognition*, pp. 5810–5818, 2017.

## A Details of the toy experiment.

1. Data domains. In this experiment, there are 5 variables: a latent binary variable  $Z$ , a binary variable  $X^*$ , an MNIST image  $\mathbf{X}$ , and two other binary variables  $y, t$ , that is:

$$\begin{aligned} Z_i, X_i^* &\in \{0, 1\} \text{ : binary values} \\ \mathbf{X}_i &\in \mathbb{R}^{28 \times 28} \text{ : an MNIST image of 0 or 1} \\ y_i, t_i &\in \{0, 1\} \text{ : binary values} \\ i &\in \{1, 2, \dots, N\}, N = 3000 \text{ : datapoint index} \end{aligned}$$

2. Data distribution.

The previously mentioned variables are sampled from the following distribution to form our synthetic dataset:

$$\begin{aligned} P[Z = 0] &= P[Z = 1] = 0.5 \\ P[t = 0 | Z = 0] &= P[t = 1 | Z = 1] = \rho_t = 0.2 \\ P[X^* = 0 | Z = 0] &= P[X^* = 1 | Z = 1] = \rho_x = 0.1 \\ \mathbf{X} &= \begin{cases} \text{a binarized image of 0 when } X^* = 0 \\ \text{a binarized image of 1 when } X^* = 1 \end{cases} \\ y &= t \oplus Z \end{aligned}$$

3. ATE computation.

As mentioned before, the definition of the Average Treatment Effect (ATE) is as follows:

$$\begin{aligned} ATE &= \mathbb{E}[ITE(x)] \\ &= \mathbb{E}[\mathbb{E}[y | \mathbf{X} = x, do(t = 1)] - \mathbb{E}[y | \mathbf{X} = x, do(t = 0)]] \end{aligned}$$

Now we consider the first term within the outer expectation:

$$\begin{aligned} &\mathbb{E}[y | \mathbf{X} = x, do(t = 1)] \\ &= 1 * P[y = 1 | \mathbf{X} = x, do(t = 1)] + 0 \\ &= \sum_z P[y = 1 | \mathbf{X} = x, do(t = 1), Z = z] \cdot \\ &\quad P[Z = z | \mathbf{X} = x, do(t = 1)] \\ &= \sum_z P[y = 1 | \mathbf{X} = x, t = 1, Z = z] \cdot P[Z = z | \mathbf{X} = x] \\ &= P[y = 1 | \mathbf{X} = x, t = 1, Z = 0] \cdot P[Z = 0 | \mathbf{X} = x] + 0 \\ &= P[Z = 0 | \mathbf{X} = x] \end{aligned}$$

where the second last equation is due to the fact that  $y = t \oplus Z$ . Similarly, we can compute the second term as:

$$\mathbb{E}[y | \mathbf{X} = x, do(t = 0)] = P[Z = 1 | \mathbf{X} = x]$$

meanwhile, according to the generation process of our data, we know that

$$\begin{aligned} P[Z = z | \mathbf{X} = x] &= \frac{P[Z = z] \cdot P[\mathbf{X} = x | Z = z]}{P[\mathbf{X} = x]} \\ &= \frac{P[Z = z] \cdot P[\mathbf{X} = x | Z = z]}{\sum_z P[Z = z] \cdot P[\mathbf{X} = x | Z = z]} \\ &= \frac{0.5 \cdot P[\mathbf{X} = x | Z = z]}{0.5 \cdot [\rho_x + (1 - \rho_x)]} \\ &= P[\mathbf{X} = x | Z = z] \\ &= P[X^* = x^* | Z = z] \end{aligned}$$

where  $x$  is an image of  $x^*$ . Plugging into the previous results, we can compute the individual treatment effect (ITE):

$$\begin{aligned}
& ITE(x) \\
&= \mathbb{E}[y|\mathbf{X} = x, do(t = 1)] \\
&\quad - \mathbb{E}[y|\mathbf{X} = x, do(t = 0)] \\
&= P[Z = 0|\mathbf{X} = x] - P[Z = 1|\mathbf{X} = x] \\
&= P[\mathbf{X} = x|Z = 0] - P[\mathbf{X} = x|Z = 1] \\
&= P[X^* = x^*|Z = 1] - P[X^* = x^*|Z = 0] \\
&= \begin{cases} 2\rho_x - 1, & \text{if } x = \text{image of 0} \\ 1 - 2\rho_x, & \text{if } x = \text{image of 1} \end{cases}
\end{aligned}$$

Notice that,

$$\begin{aligned}
P[X^* = x^*] &= \sum_z P[Z = z] \cdot P[X^* = x^*|Z = z] \\
&= 0.5 \cdot [\rho_x + (1 - \rho_x)] \\
&= 0.5
\end{aligned}$$

therefore we can plug in the previous equation and get the final result of ATE:

$$\begin{aligned}
ATE &= \mathbb{E}[ITE(x)] \\
&= \sum_x P[\mathbf{X} = x] \cdot ITE(x) \\
&= \sum_{x^*} P[X^* = x^*] \cdot ITE(\text{image of } x^*) \\
&= 0
\end{aligned}$$

## B Neural Architecture of Deep Structural Equations and Approximate Inference Networks

In this section, we will introduce the details of the architecture we used following Louizos et al. (2017). With regard to notation,  $\mathbf{X}_i$  denotes an input datapoint, that is, the feature vector,  $t_i$  is the treatment assignment,  $y_i$  denotes the corresponding outcome, and  $\mathbf{Z}_i$  is the latent hidden confounder. Each of the corresponding factors is described as:

$$\begin{aligned}
p[\mathbf{Z}_i] &= \prod_{j=1}^{D_z} \mathcal{N}(Z_{ij} | 0, 1) \\
p[t_i | \mathbf{Z}_i] &= \text{Bern}(\sigma(f_1(\mathbf{Z}_i))) \\
p[\mathbf{X}_i | \mathbf{Z}_i] &= \prod_{j=1}^{D_x} p[X_{ij} | \mathbf{Z}_i]
\end{aligned}$$

where  $\sigma(\cdot)$  is the sigmoid function, Bern is the Bernoulli distribution  $D_x, D_z$  are the dimensions of  $\mathbf{X}$  and  $\mathbf{Z}$ ,  $p[X_{ij} | \mathbf{Z}_i]$  is an appropriate probability distribution for the covariate  $j$ .

For the outcome  $y$ , if it is discrete, we parametrize its probability distribution as a Bernoulli distribution:

$$\begin{aligned}
p[y_i | t_i, \mathbf{Z}_i] &= \text{Bern}(\pi = \hat{\pi}_i) \\
\hat{\pi}_i &= \sigma(f_2(\mathbf{Z}_i, t_i))
\end{aligned}$$

and if it is continuous, we parametrize its distribution as a Gaussian with a fixed variance  $\hat{v}$ , defined as:

$$\begin{aligned}
p[y_i | t_i, \mathbf{Z}_i] &= \mathcal{N}(\mu = \hat{\mu}_i, \sigma^2 = \hat{v}) \\
\hat{\mu}_i &= f_2(\mathbf{Z}_i, t_i)
\end{aligned}$$

Here each of the  $f_i(\cdot)$  is a neural network.

For the posterior distribution, we use the following approximation:

$$q[\mathbf{Z}_i | \mathbf{X}_i, t_i, y_i] = \prod_{j=1}^{D_z} q[Z_{ij} | \mathbf{X}_i, t_i, y_i] = \prod_{j=1}^{D_z} \mathcal{N}(\mu_{ij}, \sigma_{ij}^2)$$

where

$$\mu_{ij}, \sigma_{ij}^2 = g_1(\mathbf{X}_i, y_i, t_i)$$

where each of the  $g_i(\cdot)$  is also a neural network.

The objective of this model is the variational lower bound defined as:

$$\begin{aligned} \mathcal{L} = \sum_{i=1}^N \mathbb{E}_{q[\mathbf{Z}_i | \mathbf{X}_i, t_i, y_i]} & \left[ \log p[\mathbf{Z}_i] + \log p[\mathbf{X}_i, t_i | \mathbf{Z}_i] \right. \\ & \left. + \log p[y_i | \mathbf{Z}_i, t_i] - \log q[\mathbf{Z}_i | \mathbf{X}_i, t_i, y_i] \right] \end{aligned}$$

Similar to Louizos et al. (2017), we also define the auxiliary encoders and the extra term in the variational lower bound.

Auxiliary Encoder:

$$q[t_i | \mathbf{X}_i] = \text{Bern}(\pi = \sigma(h_1(t_i)))$$

For discrete  $y_i$ :

$$\begin{aligned} q[y_i | t_i, \mathbf{X}_i] &= \text{Bern}(\pi = \hat{\pi}_i) \\ \hat{\pi}_i &= \sigma(h_2(\mathbf{X}_i, t_i)) \end{aligned}$$

for continuous  $y_i$ :

$$\begin{aligned} p[y_i | t_i, \mathbf{X}_i] &= \mathcal{N}(\mu = \bar{\mu}_i, \sigma^2 = \hat{v}) \\ \hat{\mu}_i &= h_2(\mathbf{X}_i, t_i) \end{aligned}$$

with each of  $h_i(\cdot)$  being a neural network.

Extra term of the Variational lower bound:

$$\mathcal{L}' = \sum_{i=1}^N \log q[t_i | \mathbf{X}_i] + \log q[y_i | \mathbf{X}_i, t_i]$$

Compared with Louizos et al. (2017), we applied different types of architecture for the posterior distribution  $q[\mathbf{Z}_i | \mathbf{X}_i, t_i, y_i]$ . When  $\mathbf{X}$  is an image (e.g. medical scans, patient photos), we used a convolutional neural network, which has been shown to effective in extracting information in image files (LeCun et al., 1995). But to avoid the overwhelming difference between the image and two binary variables  $t, y$ , we also apply dimension reduction techniques such as Principle Component Analysis to the embeddings of the image before feeding it into the network that is shared with  $t, y$ . In other cases, when  $\mathbf{X}$  is time-series data, (e.g. text, recording), we would change the architecture to recurrent neural networks such as Long Short Term Memory (Hochreiter & Schmidhuber, 1997).

## C Chosen features for the IHDP and STAR experiments

We experimented with the 25 original features in the IHDP experiment. We used mutual information and F-statistics between each feature and the target variable  $y$  to assess the importance of each feature in the initial 100 replicates of IHDP. While making sure that the absolute ATE errors deviate too much from the corresponding errors produced by IHDP-Full setting, we experimented with several combinations of the high ranking features to select the following 9 features in the IHDP-Mini setting

1. Feature 6: ‘sex of baby’
2. Feature 0: ‘birth-weight’
3. Feature 1: ‘b.head’
4. Feature 2: ‘preterm’
5. Feature 3: ‘birth.o’
6. Feature 8: ‘mom married?’
7. Feature 9: ‘mom’s education lower than high school?’

8. Feature 12: ‘Smoked cig during pregnancy?’
9. Feature 20: ‘harlem’

Similarly, we choose the following subset of attributes for the STAR experiment

1. Feature 2: ‘Student grade’
2. Feature 3: ‘Student class-type’
3. Feature 4: ‘Highest degree obtained by teacher’
4. Feature 5: ‘Career ladder position of teacher’
5. Feature 6: ‘Number of years of experience of teacher’
6. Feature 7: ‘Teacher’s race’
7. Feature 10: ‘Student’s gender’
8. Feature 11: ‘Student’s ethnicity’

## D Evaluating Quality of Pre-Trained Embeddings

We also build a simple neural network model that takes the CLIP embedding of an image as input and predicts the age of the person in that image. We use 5-dimensional PCA embeddings of 500 randomly chosen images of people aged 10-45 years (corresponding to the age-group in the IHDP experiment). We have an independent test dataset corresponding to 100 images chosen in a similar way. We see that the  $R^2$  value for the age prediction on test dataset is 0.45. If we increase the size of PCA embedding to 50, this  $R^2$  value increases to 0.58. Thus, it is possible to extract the age information from randomly chosen images using a simple neural network. This further supports our idea of replacing the attribute corresponding to ‘s baby’s gender with an appropriate image.

In the above setting, we also studied the classification accuracy of separate neural networks that predict gender and ethnicity from the CLIP embeddings. We saw that gender was predicted with 94% accuracy and ethnicity was predicted with 58% accuracy using a 5-dimensional PCA embedding. After increasing the size of PCA embedding to 50 dimensions, the gender prediction accuracy increased to 95% and ethnicity prediction accuracy increased to 77%.